Influence of Cryogenic Treatments on the Wear Behavior of AISI 420 Martensitic Stainless Steel
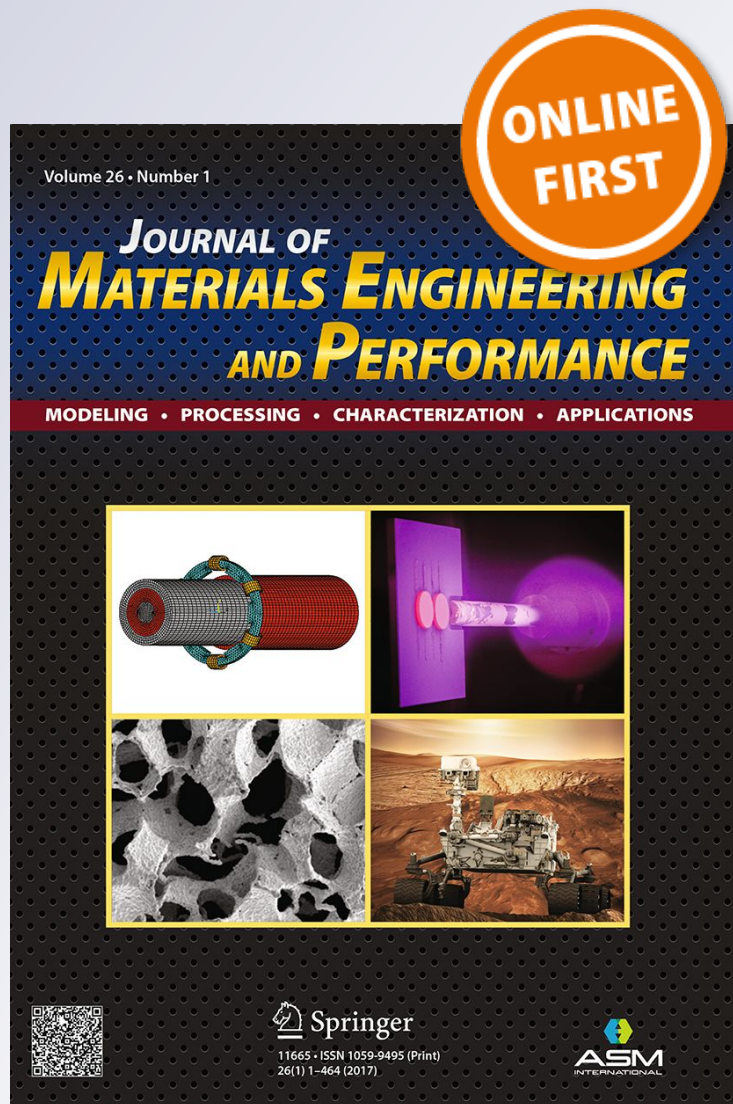
G. Prieto & W. R. Tuckart

Volume 26 · Number 1

JOURNAL OF
MATERIALS ENGINEERING
AND PERFORMANCE

MODELING · PROCESSING · CHARACTERIZATION · APPLICATIONS

ONLINE FIRST

Springer

11665 · ISSN 1059-9495 (Print)
26(1) 1–464 (2017)

ASM INTERNATIONAL

Springer

Springer

Influence of Cryogenic Treatments on the Wear Behavior of AISI 420 Martensitic Stainless Steel

G. Prieto and W.R. Tuckart

(Submitted July 22, 2016; in revised form August 19, 2017)

The objective of the present work is to characterize the wear behavior of a cryogenically treated low-carbon AISI 420 martensitic stainless steel, by means of ball-on-disk tribological tests. Wear tests were performed under a range of applied normal loads and in two different environments, namely a petrolatum bath and an argon atmosphere. Wear tracks were analyzed by both optical and scanning electron microscopy and Raman spectroscopy to evaluate wear volume, track geometry, surface features and the tribolayers generated after testing. This paper is an extension of the work originally reported in the VIII Iberian Conference of Tribology (Prieto and Tuckart, in: Ballest Jiménez, Rodríguez Espinosa, Serrano Saurín, Pardilla Arias, Olivares Bermúdez (eds) VIII Iberian conference of tribology, Cartagena, 2015). In this study, it has been experimentally demonstrated that cryogenically treated specimens showed a wear resistance improvement ranging from 35 to 90% compared to conventionally treated ones.

1. Introduction

The AISI 420 is a martensitic stainless steel, commonly used in pumping applications in the petrochemical industry, oil extraction and energy generation. Because of this, components made of AISI 420 experience severe mechanical and tribological stress; therefore, the enhancement of the wear resistance of this steel is of technological interest (Ref 1).

One of the first systematic studies regarding the influence of cryogenic treatments over a wide range of steels was performed by Ref 2. Barron reported that cryogenic treatments increased the wear resistance, particularly in the case of tool steels. Ensuing studies shown that the main effects associated with deep cryogenic treatments were the transformation of retained austenite (Ref 3-5), the precipitation and refinement of small secondary carbides (Ref 6-8) and the plastic deformation of virgin martensite (Ref 9, 10). There is a wide range of wear resistance improvements reported in the literature, ranging from 10 to 600% (Ref 6, 11, 12), depending on the processing parameters, type of alloy and testing methods. Nowadays, deep cryogenic treatments (DCT) are being increasingly used as a manufacturing technique to improve wear resistance and dimensional stability of many materials, from high-alloy tool steels to nonferrous alloys, such as copper, magnesium and aluminum alloys (Ref 13-15).

In the case of the cryotreatment of martensitic stainless steels, the published results are scarce. Reference 16 evaluated the wear performance of a cryogenically treated high C-high Cr martensitic stainless steels, reporting improvements of 44%, while (Ref 17) studied the corrosion resistance of a cryogenically treated AISI 420 steel, finding no significant difference between the behavior of DCT and CHT specimens.

In the case of the AISI 420 martensitic stainless steel, we have reported in a previous paper that the volume of retained austenite was negligible for both DCT and conventionally heat-treated (CHT) specimens (Ref 18), while in (Ref 19) we found a wear resistance improvement in DCT specimens which is further explored in this present article. Additionally, we studied the influence of cryogenic treatments on the fracture toughness of AISI 420, finding an improvement of 35% in comparison with CHT specimens (Ref 20). The purpose of this paper is to deepen the understanding of the influence of cryogenic treatments on the wear resistance of a low-carbon AISI 420 martensitic stainless steel.

2. Materials and Methods

A low-carbon AISI 420 martensitic stainless steel has been used in the present study. Its chemical composition, as presented in Table 1, was determined using a SPECTRO SPECTROMAXX (Kleve, Germany) optical emission spectrometer. The results are shown along with the reference composition taken from ASTM A276 standard (Ref 21). It should be noted that the amount of phosphorus is slightly higher than the recommended by the standard.

Ball-on-disk tests were used for wear behavior characterization. 42-mm-dia. AISI 420 disks were subjected to two different heat treatments, namely a conventional heat treatment (CHT) and a deep cryogenic treatment (DCT). For the CHT, the disks were quenched in oil from 1030 °C and afterward, tempered at 410 °C for 10 min with furnace cooling. The DCT group of disks was quenched in oil from 1030 °C and then soaked in liquid nitrogen (−196.4 °C). The cooling rate was set at −0.45 °C/s, and the soaking time at cryogenic temperature was of 2 h. Finally, the specimens were tempered at 410 °C

G. Prieto and **W.R. Tuckart**, Tribology Group, Engineering Department, Universidad Nacional del Sur, Av. Alem 1253, CP 8000 Bahía Blanca, Argentina; and Consejo Nacional de Investigaciones Científicas y Técnicas, Av. Rivadavia 1917, CP C1033AAJ Ciudad Autónoma de Buenos Aires, Argentina. Contact e-mails: german.prieto@uns.edu.ar and wtuckart@uns.edu.ar.

Table 1 AISI 420 chemical composition (wt.%)

Element	C	Cr	Mn	Si	P	S	Fe
Bar	0.17	12.83	0.76	0.55	0.05	0.017	Balance
ASTM A 276 standard [21]	0.15	12.00	1.00	1.00	0.04	0.03	Balance
	Min	14.00	Max	Max	Max	Max	
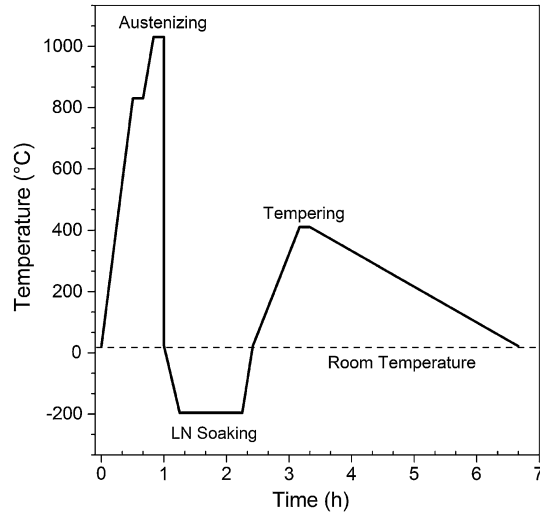
Fig. 1 Representation of the applied deep cryogenic treatment (DCT)

(heating rate ~ 9 °C/min) for 10 min and slowly cooled inside the furnace. A representation of the applied heat treatments is displayed in Fig. 1.

All disks were polished using abrasive silicon carbide papers up to 600 grit and ultrasonically cleaned with toluene for 5 min before each test. A 5-mm-dia. tungsten carbide ball was used as the counter-body (50% W/50% C, $E = 680$ GPa, $R_a = 0.05$ μm) in order to ensure that wear developed mainly in the steel disks. Roughness parameters were determined using a Hommel-Etamic T-500 (Jena, Germany) contact stylus profilometer prior testing, with a 4.8-mm cutoff length. Afterward, the Vickers hardness of the specimens was measured using an FUTURE TECH FM-300 (Kawasaki, Japan) hardness tester, with 500 gf of applied normal load.

Ball-on-disk tests were conducted under two environments following the guidelines of ASTM G 99 standard (Ref 22). The first one consisted in the immersion of the specimens and counter-bodies in a low-viscosity, additive-free liquid petrolatum bath, with a cinematic viscosity of 17 cSt at 25 °C. This lubricant was chosen to limit the introduction of additional variables to the tribosystem, such as additive reactions or hydrodynamic effects.

The lubrication regime was estimated using the (Ref 23) theory for ball-on-plane sliding conditions, according to Eq 1. This theory assumes that Reynolds hydrodynamic lubrication and Hertz elasticity are valid. This equation compares the lubricant film thickness (h) with the equivalent roughness (σ) of the tribopair, in order to assess the position of the system in the Stribeck's curve. The equivalent surface roughness is defined as

$\sigma = (R_{a1}^2 + R_{a2}^2)^{1/2}$. If $h/\sigma < 1$, then there is asperity interaction and therefore metallic wear.

$$h = 1.79 \times \alpha^{0.49} \times (\eta_0 V)^{0.68} \times R'^{0.47} \times W^{-0.07} \times E'^{-0.12}$$

$$\text{(Eq 1)}$$

where h: lubricant film thickness (m) and α: coefficient of oil viscosity. According to Ref 23, $\alpha \sim (0.6 + 0.965 \times \log(\eta_0)) \times 10^{-8}$, η_0: oil viscosity at atmospheric pressure and test temperature (cP), V: sliding velocity (m s^{-1}), R': equivalent contact radius (m), defined as: $1/R' = (1/R_1 + 1/R_2)$, W: applied normal load (N), E': equivalent elastic modulus (GPa), defined as: $1/E' = ((1 - u_1^2)/E_1) + ((1 - u_2^2)/E_2)$.

The second wear test environment was an argon atmosphere, generated inside an air-tight chamber continuously flooded with argon (99% purity) at a rate of 5 L/min. A slight positive pressure was maintained in the chamber during the tests to prevent the infiltration of air. These conditions were chosen in order to prevent the excessive oxidational wear that we found during preliminary tests (unpublished results) performed directly in air. The argon atmosphere was selected to study the tribological behavior of the specimens under dry and non-reactive conditions.

The applied normal loads for petrolatum-immersed tests were 5, 10, 15, 20 and 25 N, while the sliding speed was 0.06 m s^{-1} and the sliding distance was set at 500 m. When performing the argon tests, we were unable to measure wear at 5 N, while at 20 and 25 N, the damage was so severe that no clear conclusions could be drawn. Something similar happened when trying to reach the 500 m of sliding distance. Therefore, only the results at 10 and 15 N with 250 m of sliding distance were reported.

The theoretical (Hertzian) contact pressures ranged between 1.1 and 1.9 GPa. During the tests, the friction force was continuously measured and logged with a data acquisition system. A statistical software (Ref 24) was used to perform the regression analysis between the normal load and the wear rate.

Wear surfaces were analyzed by means of a NIKON ECLIPSE LV-100 (Melville, USA) optical microscope, while the wear measurements were taken using NIKON NIS-ELEMENTS D image processing software, at least at 30 different positions for each worn specimen. Wear volume was calculated according to the ASTM G 99 standard (Ref 22), using at least 3 valid tests for each experimental condition. Scanning electron microscopy was used to characterize the worn surfaces and subsurfaces and the resulting microstructures after each heat treatment, by means of a JEOL JSM-35CF (Tokyo, Japan) scanning electron microscope. The volume fraction of carbides was estimated from the SEM micrographies, using an open source image analysis software [Icy version 1.3.6.0 (Ref 25)] with a spot detection plug-in. This software allowed the determination of the area fraction of carbides in SEM images, as well as the mean distance between

particles, considering the average between each particle and its closest five neighbors. The carbide volume fraction has been estimated using the Delesse's Principle for stereographic relationships (Ref 26), which states that the area fraction is equal to the volume fraction.

For sub-superficial examination, worn disks were cut using a slow speed cold cut saw and carefully polished until the transversal section became tangential to the wear scar. Final polishing was made with an alumina suspension (particle size: 3 μm). Afterward, transversally cut specimens were etched using Marble reagent (10 g $CuSO_4$ in 50 ml HCl and 50 ml water), during 5 s in order to reveal the microstructural features.

X-ray diffractometry was performed using a PANalytical X'pert-MPD (Almelo, Netherlands) diffractometer (CuKα radiation—λ = 1.5405 Å) at an acceleration potential of 40 kV. The diffraction angle ranged from 20° to 120° with a 0.02° step at a speed of 0.06°/min. The diffractometer was equipped with a graphite diffracted-beam collimator and a programmable receiving slit of 0.2 mm, a divergence slit of 0.4° and an incident and collecting slit of 1°.

Raman spectra were obtained using a B&W Tek i-Raman Plus (Newark, USA) consisting of a single spectrograph (BWS465-532S), an optical microscope and a high-quantum-efficiency CCD array (2048 pixels). The spectra were excited with 532 nm radiation from a 50-mW Nd:YAG laser, and the laser beam was focused on the sample by a 100× lens to give a spot size of approximately 1 μm; the resolution was better than 3 cm^{-1}. The laser power in all cases was kept below 0.5 mW at the sample, to avoid heat damage while the acquisition time was set at 10 min.

Wear debris were collected after tests performed at 25 N load from the petrolatum bath and deposited in a glass substrate using analytical ferrography techniques. For this purpose, a PREDICT T-FM (Littleton, USA) analytical ferrograph was used. Finally, the collected wear particles were characterized by optical microscopy.

Fig. 2 SEM micrographs of (a) CHT and (b) DCT specimens showing the carbide refinement due to the cryogenic treatment

3. Results

3.1 Microstructural Characterization

The SEM micrographs of the specimens after the heat treatments are shown in Fig. 2. It can be seen that in both cases the microstructure consisted in a very fine lenticular martensitic matrix with evenly distributed globular carbides. However, due to the high amount of fine carbides in DCT specimens (Fig. 2b), it is more difficult to observe the martensitic matrix. In (Ref 18), we were able to identify the globular particles as M_7C_3 secondary carbides by means of EDS analysis.

A summary of the microstructural features of both set of specimens is presented in Table 2.

X-ray diffraction tests showed that both CHT and DCT specimens had martensitic phases (a'), while austenite could not be detected; therefore, it is inferred that its volume fraction, if it exists, is below the detection threshold of the diffractometer (>3 vol.%).

3.2 Wear Tests

Roughness measurements taken prior to the tribological testing showed that average roughness (R_a) was 0.077 ± 0.003 μ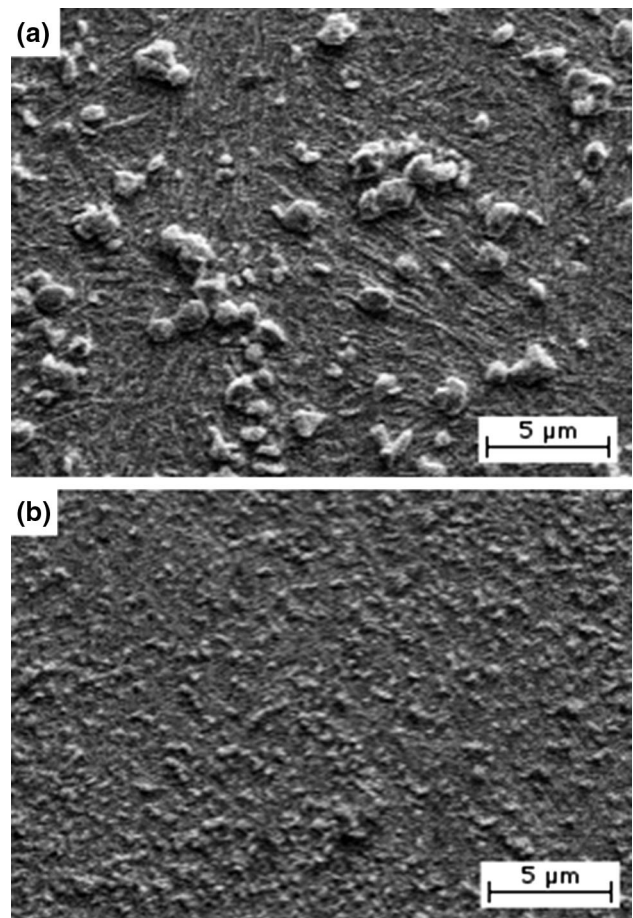m, while maximum profile peak height (R_p) was $0.290 \pm$ 0.034 μm and R_z (average of the five highest peaks and lowest valleys over the entire sampling length) was 0.644 ± 0.026 μm. Regarding the lubrication regime, the h/σ coefficient ranged between 8×10^{-5} and 7.5×10^{-5}, showing that the boundary lubrication regime was operative, and therefore, there was direct contact between the surface of the disk and the counter-body.

As it can be seen in Fig. 3, the wear rate in DCT specimens was lower than CHT ones at all the applied normal loads, both in petrolatum and in argon atmospheres. In the case of the petrolatum-immersed tests, the differences were of 35% in average. The value of the correlation coefficient (R^2) ranged between 0.93 and 0.96, meaning that the variation in applied normal load can explain more than 93% of the total variation in the wear rate. Another important feature is that the slope of the CHT fit was ~ 40% higher than that of DCT specimens (9.1×10^{-16} versus 5.3×10^{-16} m³/Nm, respectively) and that this difference was statistically significant, with an associated p value lower than 0.0001.

When analyzing the obtained results after testing in the argon atmosphere, we were unable to measure wear at loads under 10 N. In these cases, we propose that the material was still in the Stage-I (incubation) of fatigue wear (Ref 27), in which there might be some degree of plastic deformation of the surface, but without material loss or formation of free particles.

Table 2 Microstructural features of test specimens

	CHT	DCT
Carbide mean size, μm	0.87 ± 0.31	0.33 ± 0.07
Carbide volume fraction, %	16.8	11.9
Amount of carbides, units	96	656
Mean distance between carbides, μm	1.73 ± 0.72	1.37 ± 0.46
Hardness, HV	508 ± 2	534 ± 3
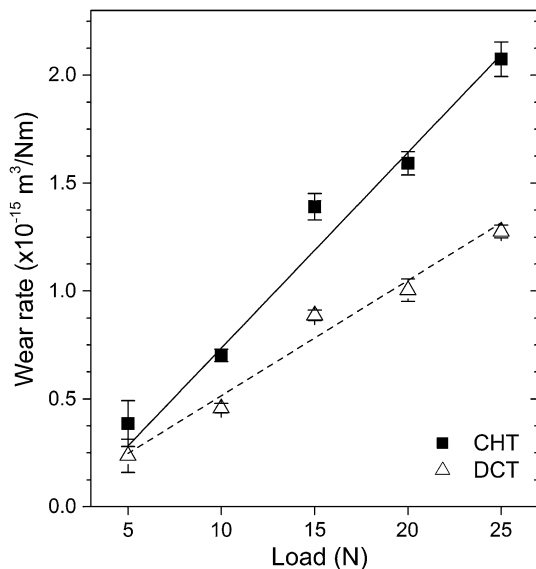
Fig. 3 Wear rate as a function of the applied normal load for petrolatum-immersed tests
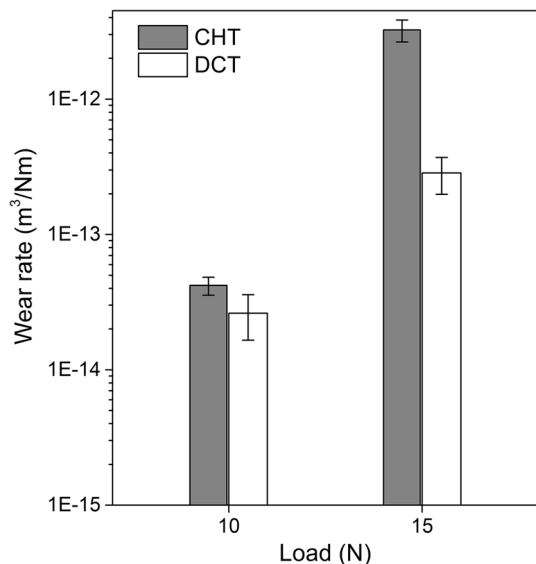
Fig. 4 Wear rate of tests performed in argon atmosphere

However, additional research should be done in order to clarify this phenomenon.

At 10 N, the wear rate markedly increased, being higher by almost an order of magnitude in comparison with the petro-latum tests (3.0×10^{-14} versus 5.5×10^{-15} m³/Nm, respectively) and at 15 N the wear rate drastically increased in the case of CHT specimens, with an increase in almost two orders of magnitude, going from 4.2×10^{-14} m³/Nm at 10 N to 3.2×10^{-12} m³/Nm at 15 N. Comparatively, the increase in wear rate for the DCT specimens was less pronounced, passing from 2.6×10^{-14} m³/Nm at 10 N to 2.8×10^{-13} m³/Nm at 15 N. It is important to note that DCT specimens had a lower wear rate than CHT ones at both load levels. These results are shown in Fig. 4, where a logarithmic scale has been used in the vertical axis in order to be able to display both groups of data.

Regarding the average friction coefficient, for the petrolatum-immersed tests, Fig. 5 shows that the coefficient of friction (CoF) of DCT specimens was slightly lower than that of CHT specimens, both in petrolatum and in argon tests. A minimum value of friction can be observed at 15 N for both groups of specimens.

The results for the argon tests show that average CoF values were higher, ranging from 0.45 to 0.60, as it was expected due to the absence of liquid lubrication or oxide layers that could act as a solid lubricant. The average CoF values were calculated after the onset of the severe damage shown in Fig. 5(b).

Figure 6 shows the friction coefficient as a function of time, both in petrolatum and in argon. Figure 6(a) corresponds to the tests performed in petrolatum at 20 N normal load, where it can be seen a steady-state region that comprises nearly 70–80% of the total sliding distance. The final stage has a similar average CoF value than the steady state one, but with a higher scatter of values. In addition, it can be seen that the CoF for the DCT specimen remains below the CHT one during the whole experiment.

The progression of the friction coefficient in argon tests is shown in Fig. 6(b). After a brief initial stable period with low values of CoF, adhesion starts to develop and the surface begins to severely damage. After the onset of heavy surface damage, the friction coefficient ranges from 0.45 to 0.60 until the end of the tests, with high scatter. In some cases, the CoF reached values close to 1.0 at the beginning of the high-friction stage, meaning that severe adhesion was taking place between the disk and the counter-body. It should be noted that the onset of this behavior was delayed in DCT specimens, as it can be seen in Fig. 6(b).

3.3 Wear Surfaces and Debris Characterization

The worn specimens were examined using optical and scanning electron microscopy. It is shown in Fig. 7(a) and (b) that the surface morphology of the wear scars is quite similar for CHT and DCT specimens, in which both groups of specimens developed a thin and compact oxide layer in the wear scar.

The increase in the normal load resulted in a widening of the scar and an increase in the oxide layer thickness. This latter
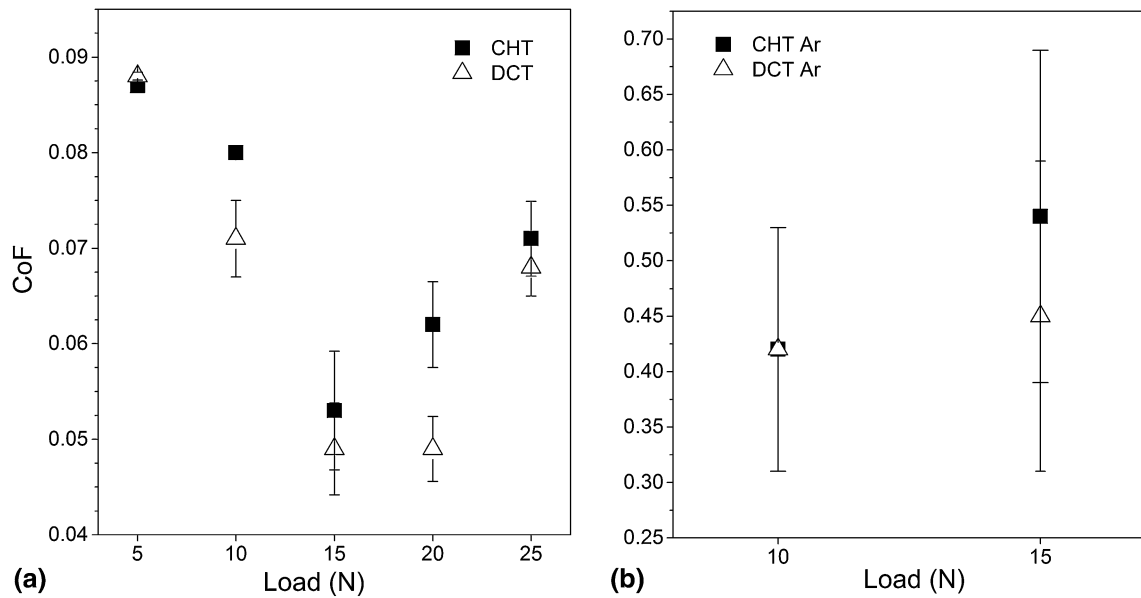
Fig. 5 Average CoF value for CHT and DCT specimens at different applied normal loads for tests performed in (a) petrolatum bath and (b) argon atmosphere
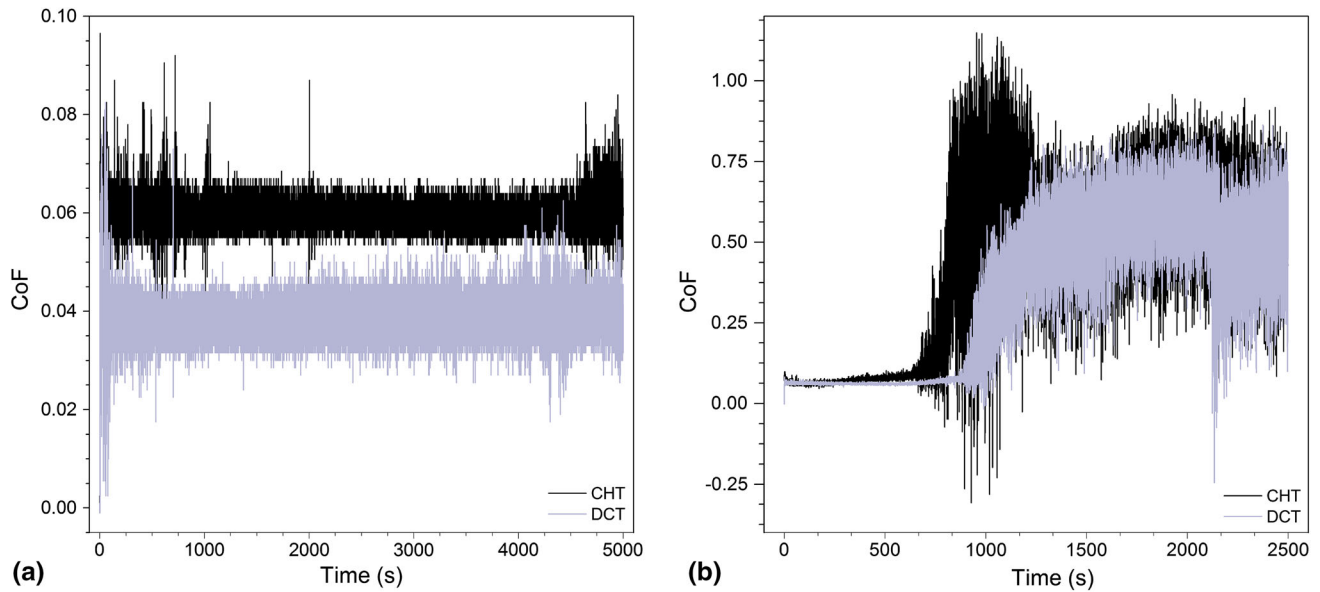

Fig. 6 Friction coefficient as a function of time for CHT and DCT specimens at (a) 20 N normal load in petrolatum and (b) 15 N normal load in argon

phenomenon was also inferred from the higher intensity of the peaks obtained with Raman spectroscopy (Fig. 13). At high load levels, mild adhesion and oxide layer transference between the disk specimens and the counter-body were observed for both CHT and DCT specimens (Fig. 8a). For the tests performed in argon, severe adhesion and material transference occurred between the disks and the counter-body (Fig. 8b).

Regarding the tests performed in argon, it can be seen in Fig. 9 that severe adhesion took place during sliding, with a high amount of plastic deformation of the surface and plate-like debris in the surrounding of the wear track. It is important to note that the worn surface appears to be metallic, without signs

of oxidation. Subsequent Raman spectroscopy tests confirmed the absence of iron oxides in the wear tracks. DCT specimens exhibited the same surface features, but with less superficial damage.

Figure 10 shows the formation of slivers along the worn surface during petrolatum-immersed tests. These superficial features are commonly associated with a ratcheting process, which are expected under unidirectional sliding tests and are the consequence of the plastic deformation of asperities. These slivers grow by plastic deformation until thin plate-like debris is formed, subsequently breaking off and detaching from the surface. From Fig. 10(b), it can be observed that the amount
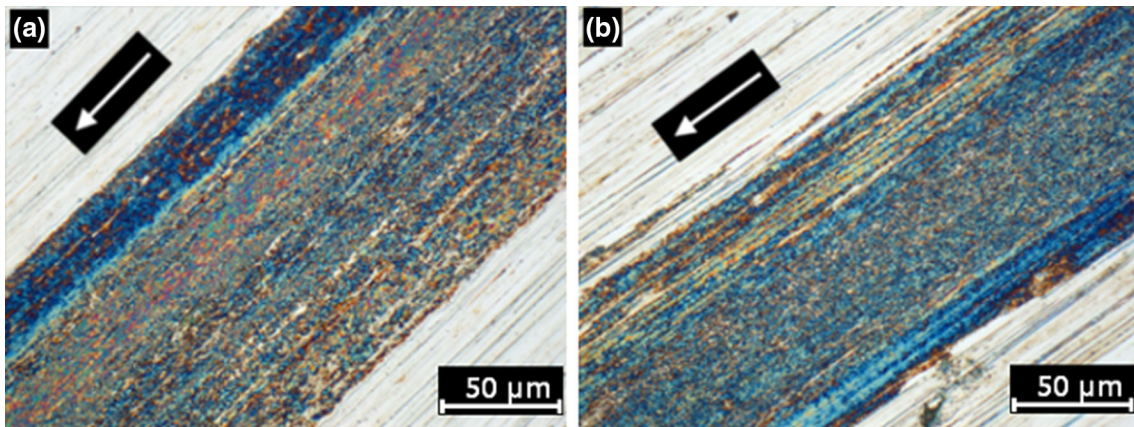
Fig. 7 Optical microscopy (OM) images of wear scars of (a) CHT at 25 N, (b) DCT at 25 N. Arrows indicate sliding direction. Tests performed in petrolatum
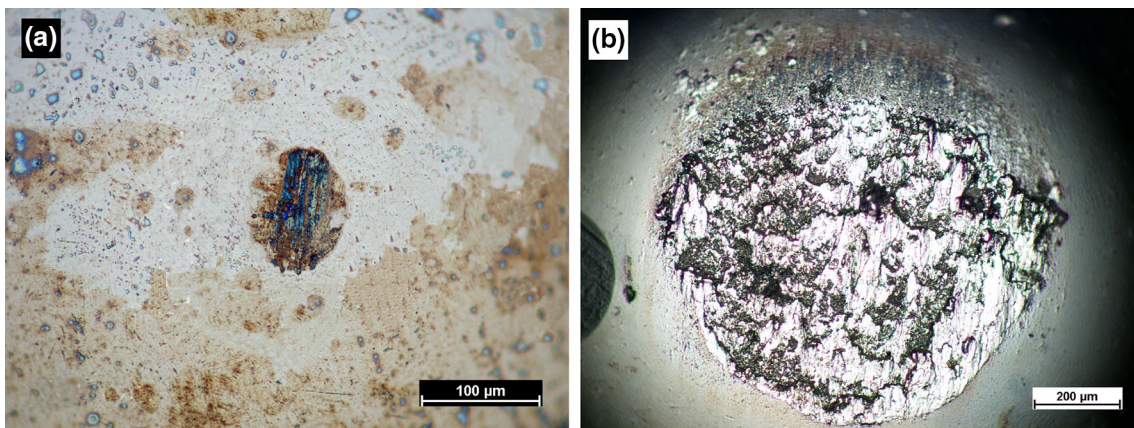

Fig. 8 OM images of the WC counter-body after testing a DCT specimen in (a) petrolatum and (b) in argon. Both tests were performed with 15 N applied normal load

and extension of slivers are less noticeable in DCT specimens. Additionally, their worn surface was more uniform compared to the one developed in CHT specimens.

Figure 11 shows the damage beneath the surface of the wear track of a CHT specimen tested in petrolatum. The martensitic microstructure has been strained along the sliding direction, displaying a fair amount of plastic deformation. Individual carbides can be seen near the surface layer, as well as a carbide cluster, that has also been distorted by the shear stresses developed during sliding. The bright zones near the surface correspond to the oxide layers, with a thickness between 20 and 60 nm. In the region highlighted by the red box, it can be seen that a sub-superficial crack had started to develop, being consistent with the ratcheting damage that can be observed in Fig. 10(a). This supports the hypothesis that the active wear mechanism is a combination of ratcheting (delamination wear) and oxide spallation.

The wear debris collected after testing CHT and DCT specimens in petrolatum are presented in Fig. 12. Bright, flake-like metallic particles can be seen in considerable quantities, as well as oxide particles ranging from 1 to 20 μm in size. This latter type of particles exhibited blue, brown and orange colorations, being consistent with the appearance of the wear surfaces presented in Fig. 7. Two distinct morphologies of metallic particles can be appreciated, one consisting of flake-like particles and the other is comprised by very narrow and curled particles which were probably generated by the detachment and cutting of the longitudinal slivers shown in Fig. 10.

Raman spectra indicated the presence of magnetite (Fe_3O_4) in the wear track surface for tests performed in petrolatum at both 25 and 5 N of normal load, as it can be seen in Fig. 13. Magnetite has its main peak typically located at 665-670 cm^{-1} (Ref 28). The base (black) line corresponds to an untested region of the specimens.

Figure 13 shows that the intensity of the peaks was slightly lower in the case of the low load tests, which can be associated with a lower oxide layer thickness (Ref 29). Also, DCT specimens showed slightly higher peak intensities at both load levels in petrolatum, meaning that oxide layers were thicker in comparison with CHT specimens, as it was also inferred from the optical microscopy images (Fig. 7). The analysis of the wear surfaces obtained in argon tests confirmed the absence of oxide layers, as there were no differences between the spectra obtained inside the wear tracks and the untested surface of the specimens.

4. Discussion

4.1 On the Effects of Cryogenic Treatments in Wear Resistance

Commonly, the soaking stage at deep cryogenic temperature lasts for a rather long time, frequently between 8 and 24 h. However, preliminary tests performed with our material with 4, 8 and 24 h of cryogenic soaking time showed that the hardness of the cryogenically treated specimens was in all cases higher than that of the conventionally treated ones, but there were no significant differences between those different cryogenic treatments (unpublished data). Therefore, in Ref 30 it was decided to shorten the duration of the treatments to 1 or 2 h of soaking time. The parameters of the applied cryogenic treatments were based on the results we obtained in Ref 18. Specifically, we selected the cryogenic treatment that yielded both the higher hardness and impact toughness values.

So far, the open literature has focused on high-alloy steels, such as tool or bearing steels in which the retained austenite contents can be as high as 27 vol.% (Ref 31). In such steels, the
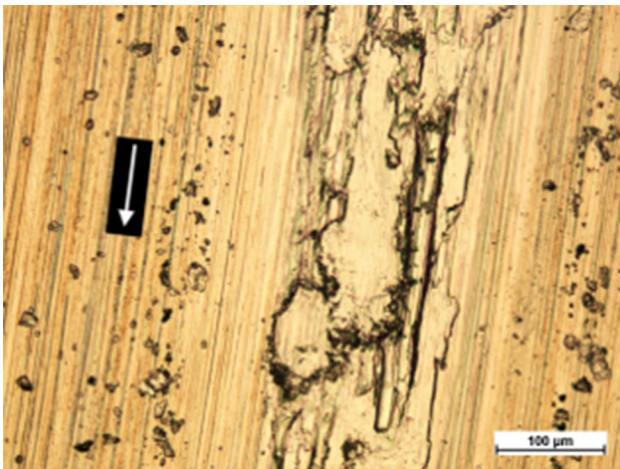

Fig. 9 OM image of a CHT specimen tested in argon atmosphere at 10 N normal load. The arrow indicates the sliding direction

high carbon content depresses the temperature at which the martensitic transformation is completed and it is commonly below room temperature. Therefore, any subsequent cooling yields a higher amount of martensitic phase after completing the heat treatment.

Figure 2 shows that both groups of specimens had martensitic microstructures. The absence of austenite peaks shows that the amount of retained austenite, if it existed, was below the detection limit of the diffractometer (< 3 vol.%). This result is consistent with those reported by Ref 32 and 33, in which AISI 420 showed no significant amounts of austenite, even in the as-quenched condition. This led us to infer that the martensite finish (M_f) temperature for AISI 420 is above room temperature. Therefore, we believe that the mechanism of deformation of virgin martensite proposed by Ref 11 does not seem to be a significant mechanism operating during the cryogenic processing of AISI 420.

Instead, we propose that the improvement in the wear resistance in DCT specimens is related to the reduction in size and to the modification of the spatial distribution of the carbides. We can back up this hypothesis with the results of Ref 7 who also focused their research on the effect of carbides over wear resistance. The results of the tribological tests they performed showed that cryogenically treated specimens had improved their wear resistance ranging from 100 to 600% compared to the conventionally treated ones. This dramatic increase in wear resistance was attributed to the precipitation of smaller carbides in DCT specimens, although the steel they used was a high-carbon-tool steel (containing high quantities of chromium, vanadium and carbon) and that the retained austenite content was estimated around 6 vol.%.

4.2 On the Operative Wear Mechanisms in Lubricated Tests

From our obtained results, we could identify that during the lubricated tests a combination of delamination wear and mild-oxidational wear has developed. The wear debris that we collected after testing the specimens (Fig. 12) is consistent with a boundary lubrication regime, where significant interaction between asperities is expected to happen. Similar results were obtained by Ref 34 during oil-immersed pin-on-disk wear tests. The development of oxidation can be related to the presence of dissolved water and oxygen in the petrolatum, which incorpo-
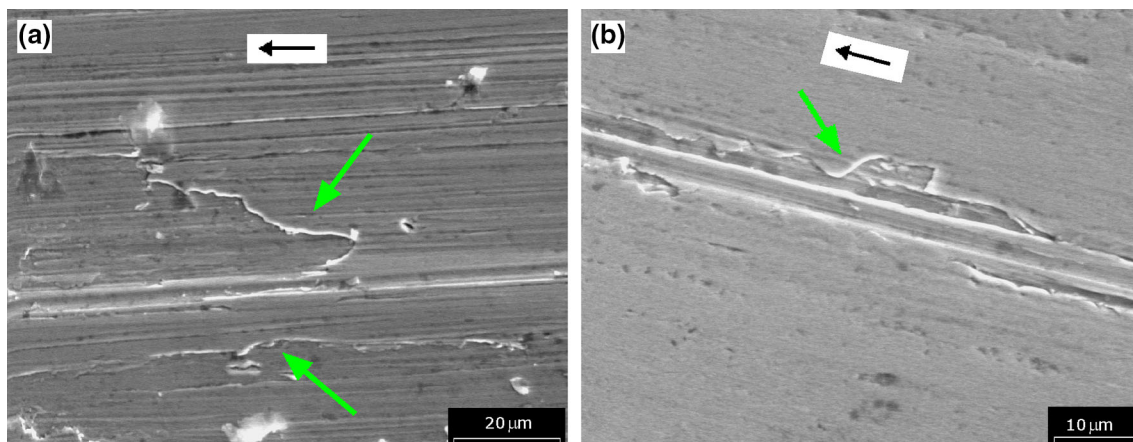

Fig. 10 SEM image of worn surfaces of (a) CHT specimen and (b) DCT specimen. In both cases, the applied normal load was 25 N and was performed in petrolatum. Green arrows show the extrusion slivers. Black arrows indicate the sliding direction
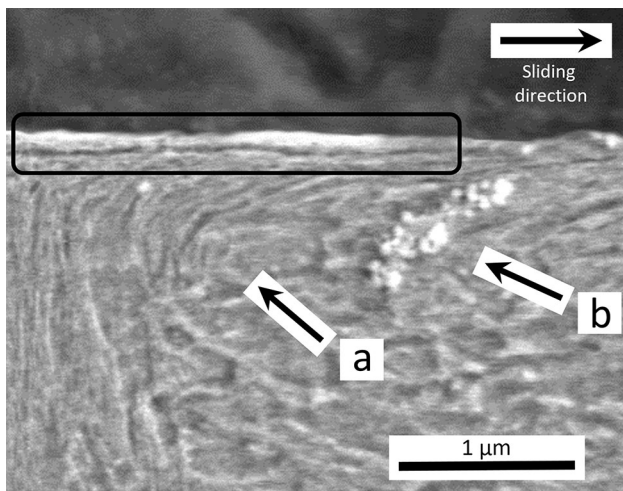
Fig. 11 Cross-sectional SEM image of a CHT specimen tested at 25 N normal load in petrolatum, showing plastic deformation of martensite laths (a) and carbide clusters (b) along with sub-superficial cracking (black box)
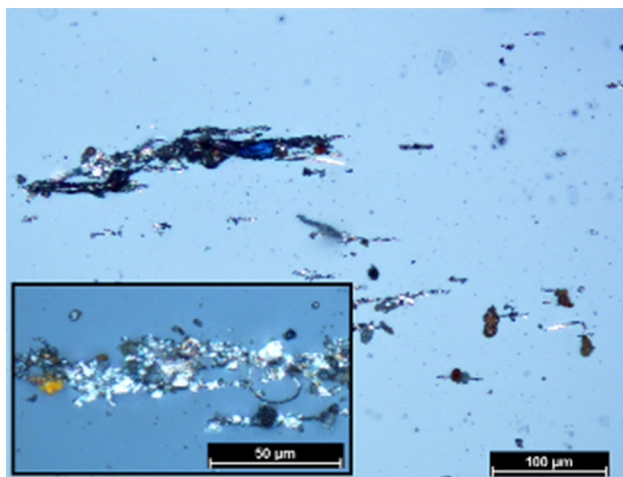

Fig. 13 Raman spectra for CHT and DCT specimens tested in petrolatum bath

Fig. 12 OM images of the wear debris collected after testing a CHT specimen at 25 N in petrolatum, consisting of metallic flake-like particles, long narrow slivers and oxide particles

rates to the lubricant from the atmosphere during the storage and the development of the wear tests (Ref 35). Although we were unable to measure the amount of dissolved water or oxygen due to a lack of the required equipment, the estimated oxygen concentration in the petrolatum should be below 9 vol.% (Ref 36).

Regarding the sub-superficial damage, (Ref 37-39) extensively studied the mechanism of delamination wear. He proposed that there is an accumulation of plastic shear deformation due to the surface traction induced by the sliding of a hard indenter on a soft surface. This accumulation process favors sub-superficial crack nucleation—the same that can be seen in Fig. 11—and when the cracks reach a certain size, they generate flake-like wear debris. This description is in strong accordance with our reported results and also with the debris presented in Fig. 12.
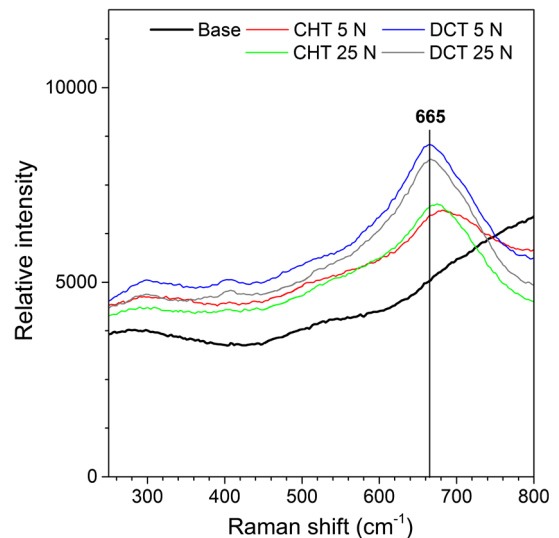
It should also be taken into account the influence of inclusion–matrix interfaces. In this sense, (Ref 37) hypothesized about its effect over crack nucleation, recognizing that this type of features acts as stress concentrators. Regarding this, Ref 40 and 41 while studying bearing steels subjected to rolling contact fatigue highlighted the importance of the influence of carbide particles in the control of the rate of damage accumulation due to ratcheting. This is because carbides act as stress concentrators, leading to nonzero mean stress cycles in their vicinity, thus promoting strain accumulation. Pandkar and collaborators studied this effect using finite elements analysis, while Bhattacharyya et al. performed accelerated rolling contact fatigue three-ball-on-rod tests, and both teams reached the conclusion that heterogeneities in the microstructure—such as carbides—cause stress concentration in their surroundings, leading to localized ratcheting. Thus, the carbide morphology modulates the hardness and the rate of localized strain accumulation.

We propose that the reduction in carbide size due to the cryogenic treatment (Fig. 2) lowers the stress concentration in their surroundings, leading to less localized plastic deformation. This accounts for less sub-superficial cracking, therefore reducing the delamination wear. However, further research should be performed in this direction.

The frictional behavior is also influenced by the formation of oxide layers. We suggest that there is a competence between the friction reduction due to the formation of oxide layers and its detachment from the surface. Both groups of specimens exhibited the development of layers mainly composed by magnetite (Fe_3O_4) (Fig. 13) which lowers the friction coefficient.

We propose that the higher CoF recorded in the tests at low normal loads (< 15 N) is due to the lack of protection from the oxide layers, while the increase in CoF at loads higher than 15 N can be attributed to the growth and subsequent detachment from the surface of the oxide layers (Fig. 6a). This phenomenon has been also described by Ref 42, p. 186.

The lower friction exhibited by DCT disks (Fig. 6 and 7) can be related to an increase in the shakedown limit due to the hardness enhancement generated by the application of the cryogenic stage. This concept was studied by Ref 43, who stated that increasing the hardness of the softer surface raises the plastic shakedown limit, thus leading to a reduction in friction and wear. The overall frictional behavior is similar to that reported by Ref 35 during lubricated pin-on-disk tests. Their reported values for the CoF were similar to the ones obtained in this present study, ranging from 0.10 to 0.13.

Additionally, we infer that the higher Raman intensities obtained from the wear tracks in DCT specimens compared to CHT ones can be associated with an increased thickness of the oxide layers (Fig. 13). We are currently investigating the corrosion behavior of DCT specimens, in order to clarify what is the dynamic of oxide formation in cryogenically treated specimens.

4.3 On the Operative Wear Mechanisms in Tests in Argon

Tests performed in argon exhibited signs of severe adhesive and delamination wear. The absence of both lubrication and oxide layers contributed to the high values of friction force that we measured (Fig. 6b). This kind of behavior, characterized by high CoFs between 0.40 and 0.60, with peaks approaching 0.90 (Fig. 7b), was also reported by Ref 44 while studying the wear of AISI 316 stainless steel in an argon atmosphere.

The delamination wear develops in a similar manner than the previously described for the lubricated tests, but with higher levels of wear and damage. This is because higher friction values lead to higher stresses and hence sub-superficial strain. In the case of argon tests, ratcheting developed more quickly than in the case of lubricated tests, as it can be inferred from the evolution of the friction coefficient (Fig. 6b) and the wear track topography (Fig. 10).

The nature of this ratcheting process should be the focus of future research, in order to clarify the role of carbides in the growth and propagation of sub-superficial cracks.

5. Conclusions

On the basis of the results obtained from the study, the wear behavior of a cryogenically treated martensitic AISI 420 stainless steel, the following conclusions may be drawn:

- The refinement in carbide size and distribution generated by the application of cryogenic treatments was sufficiently strong to improve the wear resistance of a low-carbon AISI 420 stainless steel. This improvement ranged between 35 and 90%, depending on the test environment.
- We propose that the reduction in carbide size due to cryogenic treatment diminishes sub-superficial cracking and subsequent delamination due to unidirectional sliding.
- This improvement in the tribological performance of cryogenically treated specimens is more meaningful because there was no transformation of retained austenite involved in either CHT or DCT specimens. This is in added example of the effects of cryogenic treatments on the tribological behavior of steels and strengthens the trend of using them in steels with lower-carbon contents or less amounts of alloy elements, or even with nonferrous materials.

References

1. J.K. Lo and C.H. Shek, Recent Developments in Stainless Steels, *Mater. Sci. Eng.*, 2009, **65**, p 39–104
2. R.F. Barron, Cryogenic Treatment of Metals to Improve Wear Resistance, *Cryogenics (Guildf)*, 1982, **22**, p 409–413
3. D. Das and K.K. Ray, Structure-Property Correlation of Sub-Zero Treated AISI, D2 Steel, *Mater. Sci. Eng. A*, 2012, **541**, p 45–60
4. A. Bensely, A. Prabhakaran, D. Mohan Lal, and G. Nagarajan, Enhancing the Wear Resistance of Case Carburized Steel (En 353) by Cryogenic Treatment, *Cryogenics (Guildf)*, 2005, **45**(12), p 747–754
5. V. Leskovšek, B. Ule, and B. Liščić, Relations Between Fracture Toughness, Hardness and Microstructure of Vacuum Heat-Treated High-Speed Steel, *J. Mater. Process. Technol.*, 2002, **127**(3), p 298–308
6. F. Meng, T. Kohsuke, R. Azuma, and H. Sohma, Role of Eta-Carbide Precipitations in the Wear Resistance Improvements of Fe-12Cr-Mo-V-1.4C Tool Steel by Cryogenic Treatment, *ISIJ Int.*, 1994, **34**(2), p 205–210
7. F. Meng, K. Tagashira, and H. Sohma, Wear resistance and microstructure of cryogenic treated Fe-1.4Cr-1C bearing steel, *Scr. Metall. Mater.*, 1994, **31**(7), p 865–868
8. J. Huang, Y. Zhu, X. Liao, I. Beyerlein, M. Bourke, and T. Mitchell, Microstructure of Cryogenic Treated M2 Tool Steel, *Mater. Sci. Eng. A*, 2003, **339**(1–2), p 241–244
9. A.I. Tyshchenko, W. Theisen, A. Oppenkowski, S. Siebert, O.N. Razumov, A.P. Skoblik, V.A. Sirosh, Y.N. Petrov, and V.G. Gavriljuk, Low-Temperature Martensitic Transformation and Deep Cryogenic Treatment of a Tool Steel, *Mater. Sci. Eng. A*, 2010, **527**(26), p 7027–7039
10. V.G. Gavriljuk, V.A. Sirosh, Y.N. Petrov, A.I. Tyshchenko, W. Theisen, and A. Kortmann, Carbide Precipitation During Tempering of a Tool Steel Subjected to Deep Cryogenic Treatment, *Metall. Mater. Trans. A*, 2014, **45**(5), p 2453–2465
11. A. Molinari, M. Pellizzari, S. Gialanella, G. Straffelini, and K.H. Stiasny, Effect of Deep Cryogenic Treatment on the Mechanical Properties of Tool Steels, *J. Mater. Process. Technol.*, 2001, **118**(1–3), p 350–355
12. D. Das, A.K. Dutta, and K.K. Ray, Sub-Zero Treatments of AISI, D2 Steel: Part II. Wear Behavior, *Mater. Sci. Eng. A*, 2010, **527**(9), p 2194–2206
13. M. Koneshlou, K. Meshinchi Asl, and F. Khomamizadeh, Effect of Cryogenic Treatment on Microstructure, Mechanical and Wear Behaviors of AISI, H13 Hot Work Tool Steel, *Cryogenics (Guildf)*, 2011, **51**(1), p 55–61
14. K. Gu, H. Zhang, B. Zhao, J. Wang, Y. Zhou, and Z. Li, Effect of Cryogenic Treatment and Aging Treatment on the Tensile Properties and Microstructure of Ti–6Al–4V Alloy, *Mater. Sci. Eng. A*, 2013, **584**, p 170–176
15. Y. Liu, S. Shao, C. Xu, X. Yang, and D. Lu, Enhancing Wear Resistance of Mg-Zn-Gd Alloy by Cryogenic Treatment, *Mater. Lett.*, 2012, **76**, p 201–204
16. J.D. Darwin, D. Mohan Lal, and G. Nagarajan, Optimization of Cryogenic Treatment to Maximize the Wear Resistance of 18% Cr Martensitic Stainless Steel by Taguchi Method, *J. Mater. Process. Technol.*, 2008, **195**(1–3), p 241–247
17. W. Wei, V. Srinivasan, S. Siva, A. Bensely, M. Lal, and A. Alfantazi, Corrosion Behavior of Deep Cryogenically Treated AISI, 420 and AISI, 52100 Steel, *Corros. Sci.*, 2014, **9312**, p 708–720
18. G. Prieto, J.E. Perez Ipiña, and W.R. Tuckart, Cryogenic Treatments on AISI, 420 Stainless Steel: Microstructure and Mechanical Properties, *Mater. Sci. Eng. A*, 2014, **605**, p 236–243
19. G. Prieto, W.R. Tuckart, Wear Behavior of Cryogenically Treated AISI 420 Martensitic Stainless Steel, in: A.E. Ballest Jiménez, T. Rodríguez

Espinosa, N. Serrano Saurín, J. Pardilla Arias, M.D. Olivares Bermúdez (Eds.), *VIII Iberian Conference of Tribology* (Universidad Politécnica de Cartagena, Cartagena, España, 2015), pp. 68–75

20. G. Prieto, W.R. Tuckart, and J.E. Perez Ipiña, Influence of a Cryogenic Treatment on the Fracture Toughness of AISI, 420 Martensitic Stainless Steel, *Mater. Tehnol.*, 2017, **51**, p 591

21. ASTM A276/A276M-16a, Standard Specification for Stainless Steel Bars and Shapes, ASTM International, West Conshohocken, PA, 2016

22. ASTM G99-17, Standard Test Method for Wear Testing with a Pin-on-Disk Apparatus ASTM International, West Conshohocken, PA, 2017

23. I.M. Hutchings, *Tribology: Friction and Wear of Engineering Materials*, Butterworth-Heinemann Ltd, Oxford, 1992

24. J.A. Di Rienzo, F. Casanoves, M.G. Balzarini, L. Gonzalez, M. Tablada, and C.W. Robledo, *Infostat [Computer software]*, Universidad Nacional de Córdoba, Córdoba, 2012

25. F. de Chaumont et al., Icy: An Open Bioimage Informatics Platform for Extended Reproducible Research, *Nat. Methods*, 2012, **9**, p 690–696

26. E.E. Underwood, *Quantitative stereology*, Addison-Wesley, Boston, 1970

27. R.G. Bayer, *Mechanical Wear Fundamentals and Testing, Revised and Expanded*, CRC Press, New York, 2004

28. D.L.A. de Faria, S.V. Silva, and M.T. de Oliveira, Raman Microspectroscopy of Some Iron Oxides and Oxyhydroxides, *J. Raman Spectrosc.*, 1997, **28**, p 873–878

29. E. Ramanaidou, M. Wells, I. Lau, and C. Laukamp, Characterization of Iron Ore by Visible and Infrared Reflectance and, Raman Spectroscopies, in: L. Lu (Ed.), *Iron ore* (Elsevier 2015), pp. 191–228

30. G. Prieto, Estudio del efecto de tratamientos térmicos de criogenia sobre el comportamiento tribológico y la tenacidad a la fractura del acero AISI 420, Universidad Nacional del Sur (2016)

31. V. Leskovšek, M. Kalin, and J. Vižintin, Influence of Deep-Cryogenic Treatment on Wear Resistance of Vacuum Heat-Treated HSS, *Vacuum*, 2006, **80**(6), p 507–518

32. S. Da Sun, D. Fabijanic, A. Ghaderi, M. Leary, J. Toton, S. Sun, M. Brandt, and M. Easton, Microstructure and Hardness Characterisation of Laser Coatings Produced with a Mixture of AISI, 420 Stainless Steel and Fe-C-Cr-Nb-B-Mo Steel Alloy Powders, *Surf. Coat. Technol.*, 2016, **296**, p 76–87

33. S. Dodds, A.H. Jones, and S. Cater, Tribological Enhancement of AISI, 420 Martensitic Stainless Steel Through Friction-Stir Processing, *Wear*, 2013, **302**(1–2), p 863–877

34. C.Q. Yuan, Z. Peng, X.C. Zhou, and X.P. Yan, Effects of Temperature on Sliding Wear Process Under Contaminated Lubricant Test Conditions, *Wear*, 2004, **257**, p 812–822

35. Z. Cai, Y. Zhou, and J. Qu, Effect of Oil Temperature on Tribological Behavior of a Lubricated Steel-Steel Contact, *Wear*, 2015, **332–333**, p 1158–1163

36. R. Rodnight, Appendix—Manometric Determination of the Solubility of Oxygen in Liquid Paraffin, Olive Oil and Silicone Fluids, *Biochem. J.*, 1954, **57**(4), p 661

37. N.P. Suh, An Overview of the Delamination Theory of Wear, *Wear*, 1977, **44**, p 1–16

38. N.P. Suh, The Delamination Theory of Wear, *Wear*, 1973, **25**(1), p 111–124

39. N.P. Suh and H.-C. Sin, The Genesis of Friction, *Wear*, 1981, **69**(1), p 91–114

40. A.S. Pandkar, N. Arakere, and G. Subhash, Microstructure-Sensitive Accumulation of Plastic Strain Due to Ratcheting in Bearing Steels Subject to Rolling Contact Fatigue, *Int. J. Fatigue*, 2014, **63**, p 191–202

41. A. Bhattacharyya, G. Subhash, and N. Arakere, Evolution of Subsurface Plastic Zone Due to Rolling Contact Fatigue of M-50 NiL Case Hardened Bearing Steel, *Int. J. Fatigue*, 2014, **59**, p 102–113

42. P.J. Blau, *Friction Science and Technology: From Concepts to Applications*, CRC Press, New York, 2008

43. Y. Xie and J.A. Williams, The Prediction of Friction and Wear when a Soft Surface Slides Against a Harder Rough Surface, *Wear*, 1996, **196**, p 21–34

44. A.F. Smith, Influence of Environment on the Unlubricated Wear of 316 Stainless Steel at Room Temperature, *Tribol. Int.*, 1986, **19**, p 3–10